*Small Structures*

small structures

www.small-structures.com

RESEARCH ARTICLE OPEN ACCESS

# Antimony-Based Lead-Free Perovskite Thin Films for Highly Sensitive Ammonia ($NH_3$) Gas Detection

Jae Ho Kim[1] | Gyumok Lim[2,3] | Hyunwoo Jang[4] | Yubin Kim[2] | Cheyeon Kim[2] | Jongbok Kim[3] | Tanzeela Yousaf[5] | Jan Seidel[5] | Jincheol Kim[5,6] | Jinsung Kwak[7] | Hyung Woo Lee[1,8,9,10] | Youngho Kang[4] | Myungkwan Song[2]

[1]Humanoid olfactory display Innovation research Center, Pusan National University, Busan, Republic of Korea | [2]Energy & Environmental Materials Research Division, Korea Institute of Materials Science (KIMS), Gyeongsangnam-do, Republic of Korea | [3]Department of Materials Science and Engineering & Department of Energy Engineering Convergence, Kumoh National Institute of Technology, Gyeongsangbuk-do, Republic of Korea | [4]Department of Materials Science and Engineering, Incheon National University, Incheon, Republic of Korea | [5]School of Materials Science and Engineering, University of New South Wales, Sydney, NSW, Australia | [6]School of Engineering, Macquarie University, Sydney, NSW, Australia | [7]Department of Physics, Changwon National University, Gyeongsangnam-do, Republic of Korea | [8]Department of Nano Fusion Technology, Pusan National University, Busan, Republic of Korea | [9]Research Center of Energy Convergence Technology, Pusan National University, Busan, Republic of Korea | [10]Research Institute for Convergence of Biomedical Science and Technology, Pusan National University Yangsan Hospital, Yangsan-si, Republic of Korea

**Correspondence:** Hyung Woo Lee (lhw2010@pusan.ac.kr) | Youngho Kang (youngho84@inu.ac.kr) | Myungkwan Song (smk1017@kims.re.kr)

**Received:** 30 January 2026 | **Revised:** 14 May 2026 | **Accepted:** 8 June 2026

**Keywords:** ammonia ($NH_3$) | antimony (Sb)-based perovskite | eco-friendly | gas sensor | lead-free

## ABSTRACT

Antimony (Sb)-based perovskite materials have emerged as promising alternatives to Pb halide perovskites for gas-sensing applications, offering reduced toxicity while maintaining high environmental sensitivity. Herein, we report a novel Sb-based perovskite, formamidinium $(FA)_3Sb_2Br_9$, as an environmentally friendly candidate for ammonia ($NH_3$) detection. $FA_3Sb_2Br_9$ can be synthesized via a simple solution-based method, and it exhibits high selectivity and sensitivity toward $NH_3$. Gas-sensing measurements revealed that the device showed a markedly higher response to $NH_3$ than to other gases, such as $NO_x$, CO, methanol, and methane. The device achieves a maximum gas response ($R = \Delta I(I_t - I_{air})/I_{air} \times 100$ (%) = 235, at 100 ppm $NH_3$), with a short response/recovery time (13/289 s), a low detection limit of 1 ppm, and excellent reversibility. Furthermore, the $FA_3Sb_2Br_9$ sensor demonstrated a linear dependence on the $NH_3$ concentration, long-term stability under ambient conditions over several months, and outstanding repeatability. These findings highlight the potential of Sb-based perovskites as promising materials for high-performance, Pb-free $NH_3$ gas sensors.

## 1 | Introduction

Pb halide perovskites have garnered significant attention in recent years because of their remarkable electronic and optoelectronic properties, including defect tolerance, suitable bandgap, strong absorbance, high carrier mobility, and long diffusion length [1–3]. These properties make them attractive for a broad range of applications, such as solar cells [4], light-emitting diodes [5], lasers [6], and photodetectors [7]. In addition to these optoelectronic applications, the unique responsiveness of perovskite materials to environmental stimuli has provided new opportunities for sensor technologies where changes in their electrical or optical properties can be exploited. Perovskite-based sensors are capable of detecting humidity [8, 9], oxygen ($O_2$) [10], hydrogen sulfide ($H_2S$) [11], nitrogen dioxide ($NO_2$) [12], carbon monoxide (CO) [13], and ammonia ($NH_3$) [14–16].

Recently, eco-friendly energy alternatives, particularly those aimed at achieving C neutrality, have received growing global interest. $NH_3$ has emerged as a promising carrier for hydrogen

Jae Ho Kim, Gyumok Lim, and Hyunwoo Jang contributed equally to this work.

($H_2$) storage and transportation, owing to its high hydrogen density and ease of liquefaction [17]. However, despite these advantages, $NH_3$ presents serious environmental and health hazards, even at low concentrations. Human exposure limits are strictly regulated, with guidelines recommending short-term (15 min) and long-term (8 h) exposure limits of 35 and 25 ppm, respectively [18, 19]. At these concentrations, $NH_3$ is often undetectable by the human olfactory system, which emphasizes the need for reliable and sensitive detection methods to enable timely intervention. Therefore, the accurate detection and management of $NH_3$ leakage are crucial for ensuring its safe and effective use in industrial environments [20].

Compared with conventional $NH_3$-sensing materials such as graphene, transition metal dichalcogenides (TMDs), MXenes, and metal oxides, halide perovskites offer several unique advantages for chemiresistive gas sensing. Although graphene- and MXene-based sensors exhibit high sensitivity at room temperature, they often suffer from limited selectivity, slow recovery behavior, or environmental instability [21, 22]. Metal oxide-based sensors generally require elevated operating temperatures to achieve sufficient sensing performance [23]. In contrast, halide perovskites possess a soft ionic lattice, high defect tolerance, and strong electronic polarizability, which enable efficient modulation of carrier transport upon interaction with polar gas molecules. In particular, electron-donating $NH_3$ molecules can strongly perturb the electronic structure of halide perovskites through reversible ionic and electronic interactions, resulting in pronounced conductivity changes even at relatively low concentrations. Furthermore, the solution processability and tunable chemical compositions of halide perovskites provide additional advantages for the fabrication of low-cost and highly tailorable gas sensor platforms.

Thus, various materials have been investigated to improve the performance of $NH_3$ gas sensors. Ayesh et al. reported that a $FA(CH(NH_2))PbBr_3$-based sensor exhibited response and recovery times of 0.2 and 0.6 min, respectively, at 0.5 ppm of $H_2S$ [11]. Zhao et al. reported a $MA(CH_3NH_3)PbI_3$-based $NH_3$ sensor that displayed a visible color change from brown to colorless (400–800 nm) within 1 s of exposure to 3% $NH_3$ [14]. Jiao et al. reported a $MAPbBr_{3-x}I_x$-based sensor with a short response–recovery time (<20 s) when exposed to 500 ppm of $NH_3$ at room temperature [15]. These studies highlight the remarkable sensitivity of Pb halide perovskite materials for gas detection, making them attractive for applications in environmental monitoring, industrial safety, and healthcare.

Despite these promising results, the commercial utilization of Pb halide perovskites is hindered by the toxicity of Pb and its sensitivity to environmental factors such as humidity and oxygen, leading to instability [24–26]. Consequently, increasing research efforts have focused on developing low-toxicity alternatives to address these challenges. Among the various Pb-free halide perovskite candidates, Sb-based bromide perovskites are particularly attractive because of their favorable environmental stability and intrinsic p-type electronic characteristics associated with Sb-related lone-pair states. Compared with many previously reported Bi-based perovskites, Sb-based systems can exhibit more effective carrier transport modulation and defect-mediated conductivity changes, which are advantageous for chemiresistive sensing applications [27]. These characteristics make Sb-based halide perovskites promising candidates for detecting electron-donating gases such as $NH_3$ through conductivity modulation mechanisms. In particular, antimony ion ($Sb^{3+}$) and bismuth ion ($Bi^{3+}$) have emerged as potential substitutes because of their isoelectronic configuration with tin ion ($Sn^{2+}$) and lead ion ($Pb^{2+}$), respectively [28–30]. Among the Pb-free alternatives, most $NH_3$ sensors reported to date are based on Bi-based perovskites. For instance, Li et al. reported that a $(phenethylammonium)_3Bi_2Br_9$-based sensor exhibited a response time of 1.76 s upon exposure to 30 ppm $NH_3$ [31]. Bhosale et al. reported that an $MA_3Bi_2I_9$ perovskite thin film-based $NH_3$ sensor exhibited excellent repeatability with response and recovery times of 0.14 and 8.15 s, respectively, at 6 ppm of $NH_3$ [32]. Additionally, Jiao et al. demonstrated a $Cs_3Bi_2I_6Br_3$-based inorganic perovskite sensor with a response value of 11.8 ($R = R_a/R_g$) at 500 ppm $NH_3$, a reaction time under 20 s, a recovery time over 120 s, and operational stability for approximately 14 days [33].

In this study, we report the novel application of a Pb-free Sb-based perovskite, $FA_3Sb_2Br_9$, as an active sensing material for $NH_3$ detection. An $FA_3Sb_2Br_9$ thin film-based $NH_3$ sensor was fabricated via a simple solution-based spin-coating method and thoroughly characterized. The sensor exhibited a high response value of 235–100 ppm of $NH_3$ (Response $= \Delta I(I_t - I_{air})/I_{air} \times 100$ (%)), with response and recovery times of 13 and 289 s, respectively. In addition to its sensitivity, the sensor demonstrated excellent selectivity against interfering gases, such as CO, $NO_x$, and methanol, along with good reversibility, repeatability, and long-term stability over several months under ambient conditions. Furthermore, we proposed a plausible sensing mechanism for the interactions between $FA_3Sb_2Br_9$ and $NH_3$ molecules.

## 2 | Results and Discussion

### 2.1 | Materials Characterization

Figure 1b shows real images of the $FA_3Sb_2Br_9$ thin films under ambient conditions (left), after exposure to 100 ppm $NH_3$ (middle), and after the recovery process (right). No significant color change was observed in the yellow $FA_3Sb_2Br_9$ films treated with 100 ppm $NH_3$. However, after 10 min of exposure to a higher concentration of 1000 ppm $NH_3$, the yellow films gradually became transparent (Figure S1). These findings are consistent with those of Bhosale et al., who demonstrated that the colorimetric and structural properties of $MA_3Bi_2I_9$ are influenced by the $NH_3$ concentration [28]. The morphologies of the fabricated $FA_3Sb_2Br_9$ perovskite thin film, the sample treated with 100 ppm $NH_3$, and the recovered film were analyzed using scanning electron microscopy (SEM), as shown in Figure 1c–e. Although no perceptible color change was observed with the naked eye, the SEM images revealed that the starfish-like microstructure of the $FA_3Sb_2Br_9$ thin film emerged during $NH_3$ exposure and recovery. As shown in Figure 1c, the pristine $FA_3Sb_2Br_9$ film comprises hexagonal microcrystals with an average diameter of approximately 20 μm. These crystals were nonuniformly deposited on the surface. Notably, upon exposure to $NH_3$, the hexagonal microcrystals undergo a distinct morphological transformation into starfish-like structures, as shown in Figure 1d. This transformation was attributed to structural changes induced

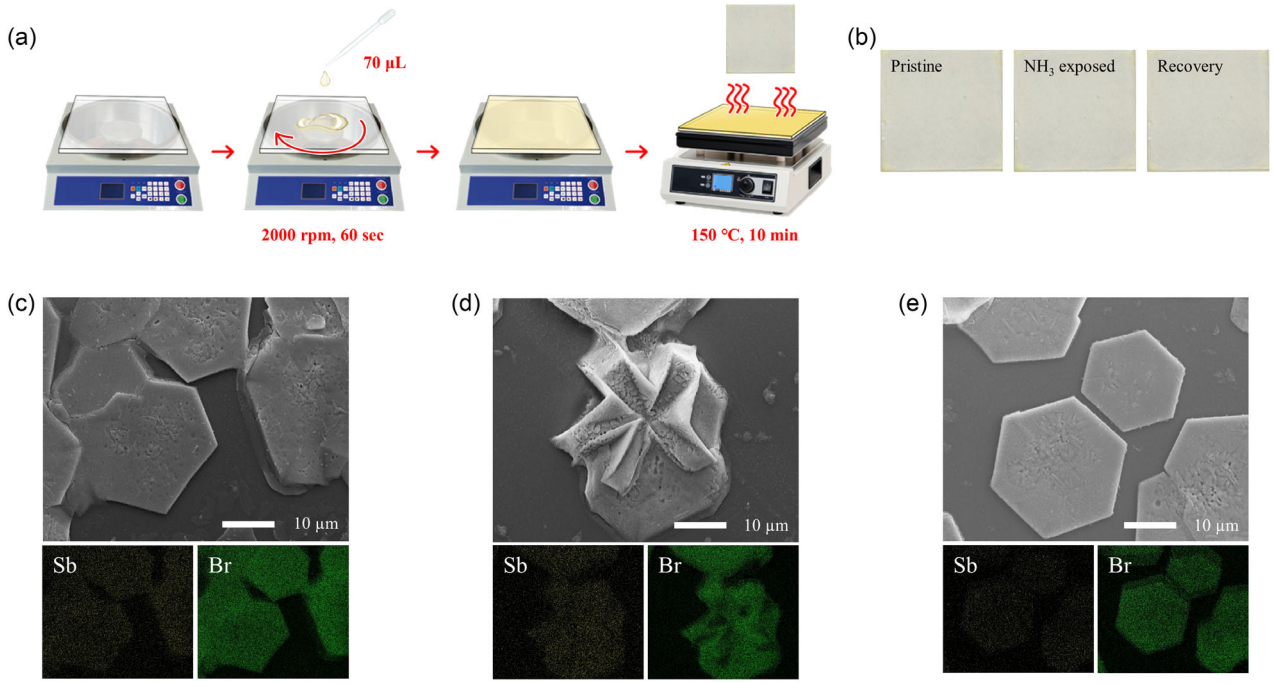


**FIGURE 1** | (a) Schematic of the $FA_3Sb_2Br_9$ thin film fabrication process. The final thin film is shown on the right end of the hot plate. Characterization of $FA_3Sb_2Br_9$ thin films in pristine, $NH_3$-exposed (100 ppm, 10 min), and recovered states: (b) photographic images of the films: pristine (left), after $NH_3$ exposure (middle), and after recovery in air (right). (c)–(e) SEM images and corresponding EDS elemental mapping of (c) pristine, (d) $NH_3$-exposed, and (e) recovered films, with uniform distribution of Sb and Br throughout the grains.

by $NH_3$. After the recovery process in ambient air, the SEM image in Figure 1e shows the reappearance of the original hexagonal morphology, indicating the reversibility of the structural changes. The elemental distributions within the thin films at each stage were examined using energy dispersion spectroscopy (EDS). Figure 1c–e confirms that Sb and Br are uniformly distributed throughout the hexagonal grains in all samples.

To investigate the influence of $NH_3$ concentration on the surface crystal structure of the $FA_3Sb_2Br_9$ thin films, the thin films were exposed to 1000 ppm $NH_3$ followed by a recovery process in ambient air. The corresponding SEM images are presented in Figure S2. As shown in Figure S2a, the pristine sample exhibits hexagonal microcrystals similar to those in Figure 1c. Upon exposure to high $NH_3$ concentrations, these hexagonal structures transform into novel leaf-like morphologies, as shown in Figure S2b. After recovery in air, small spherical crystals appeared on the substrate surface, which were distinctly different from the original hexagonal configuration, as shown in Figure S2c. In addition, Figure S2 shows the elemental mapping data of the films under 1000 ppm $NH_3$ conditions, confirming that C, N, Sb, and Br were uniformly distributed throughout the crystal structures, consistent with the observations at 100 ppm. These findings demonstrate that the surface morphology and crystal structure of $FA_3Sb_2Br_9$ thin films vary significantly depending on the concentration of $NH_3$ exposure.

Figure 2a shows the X-ray diffraction (XRD) patterns of the $FA_3Sb_2Br_9$ thin films in their pristine, $NH_3$-exposed, and recovered states, demonstrating their crystalline characteristics. While the XRD pattern of $FA_3Sb_2Br_9$ has not been previously reported, it closely resembles that of $Cs_3Sb_2Br_9$, suggesting a similar crystal structure [34]. This is understandable given the comparable ionic radii of $Cs^+$ (~0.17 nm) and $FA^+$ (0.19–0.22 nm) ions [35, 36]. The main diffraction peaks located at 17.7°, 26.7°, and 54.9° correspond to the (002), (201), and (402) crystal planes, respectively. The XRD analysis confirms that the perovskite microplates have a trigonal crystal structure with lattice parameters of $a = b = 7.93$ Å, $c = 9.716$ Å, and angles of $\alpha = \beta = 90°$, $\gamma = 120°$, consistent with the space group $P\bar{3}$ m1 (164). These structural characteristics and surface crystal shapes agree with those reported for $Cs_3Sb_2Br_9$ [34]. Importantly, the XRD patterns of the thin films exposed to 100 ppm $NH_3$ and those following recovery exhibited no significant changes, suggesting that the hexagonal crystal structure was preserved, as also supported by the SEM analysis. The locally formed starfish-like crystals did not induce notable alterations in the XRD patterns. In contrast, exposure to 1000 ppm $NH_3$ led to the emergence of new diffraction peaks at 18.9°, 22.0°, 28.0°, 31.2°, 38.5°, 44.7°, and 50.3° (Figure S3a), indicating a distinct structural transformation. Moreover, the XRD pattern of the recovered film after 1000 ppm exposure exhibited a completely different profile, suggesting irreversible changes in the crystal structure under high $NH_3$ concentrations. Therefore, these SEM and XRD findings collectively suggest that $FA_3Sb_2Br_9$ thin films can efficiently respond to and recover from exposure to relatively low $NH_3$ concentrations, such as 100 ppm. In contrast, exposure to higher concentrations, specifically 1000 ppm $NH_3$, induced irreversible structural changes in the films, preventing full recovery to the original crystalline state.

To investigate the optical response of the $FA_3Sb_2Br_9$ thin films to $NH_3$ exposure, UV–visible absorption spectra were measured in the wavelength range of 300–800 nm, as shown in Figure 2b.

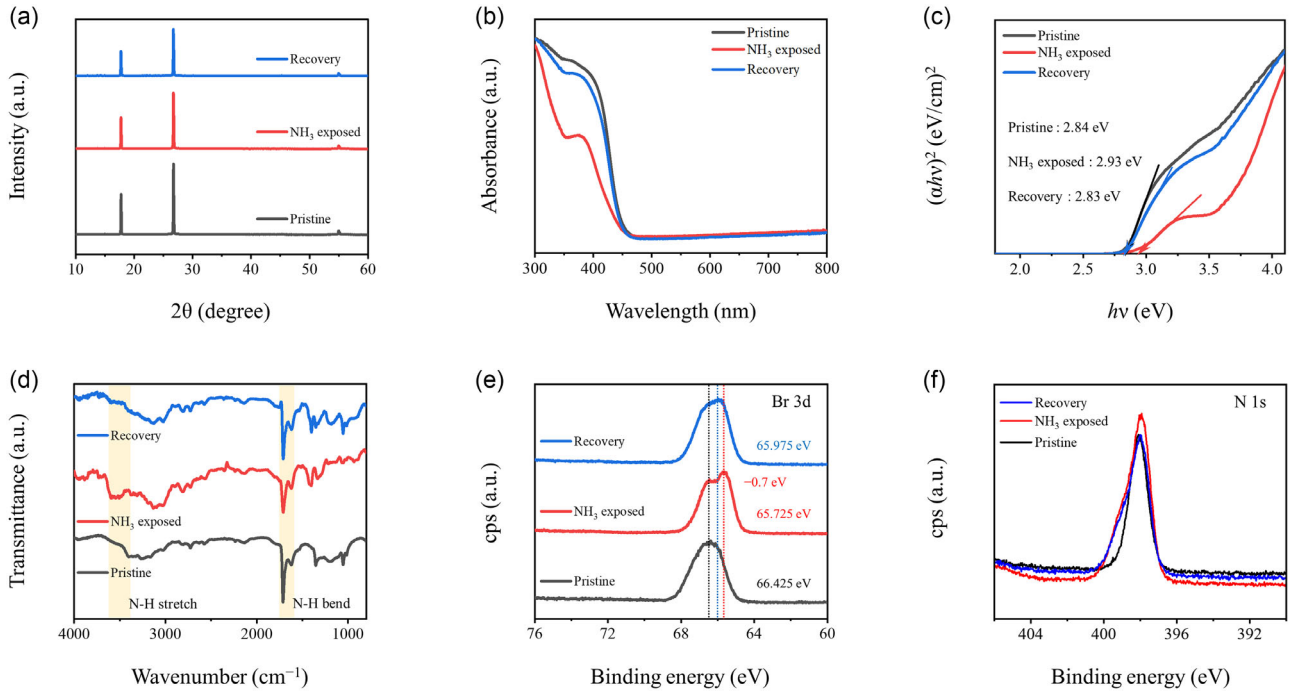


**FIGURE 2** | Characterization of $FA_3Sb_2Br_9$ thin films in pristine, $NH_3$-exposed (100 ppm), and recovered states: (a) XRD patterns, (b) UV–visible absorption spectra, (c) Tauc plots, and (d) FT-IR spectra. XPS spectra of $FA_3Sb_2Br_9$ thin films under high $NH_3$ exposure (100 ppm): (e) Br 3*d* and (f) N 1*s*.

The pristine film exhibited strong absorption between 300 and 450 nm, with a sharp absorption edge near 430 nm and negligible absorbance beyond 450 nm. Upon exposure to $NH_3$, the absorbance in the visible region, particularly at approximately 400 nm, decreases significantly, indicating a perturbation in the electronic structure or surface morphology of the film. After recovery in ambient air, the absorbance near 400 nm increased again and approached that of the pristine state, suggesting that the optical properties of $FA_3Sb_2Br_9$ could be restored at low $NH_3$ concentrations. These optical absorption changes are consistent with the morphological observations from SEM analysis and further support the potential of this material for reversible $NH_3$-sensing applications under mild conditions.

To evaluate the effect of $NH_3$ exposure on the optical bandgap of the $FA_3Sb_2Br_9$ thin films, Tauc plot analysis was performed based on the UV–visible absorption spectra. Figure 2c displays the plots of $(\alpha h\nu)^2$ versus photon energy ($h\nu$), where $\alpha$ is the absorption coefficient and $\nu$ is the optical frequency. The bandgap energies were estimated by extrapolating the linear portions of the curves to the energy axis. The calculated optical bandgaps of the pristine, $NH_3$-exposed, and recovered films were 2.84, 2.93, and 2.83 eV, respectively, indicating that $NH_3$ exposure induces a blueshift in the bandgap, which is nearly reversible after recovery under ambient conditions.

To further investigate the impact of higher $NH_3$ concentrations on the optical properties of the $FA_3Sb_2Br_9$ thin films, UV–visible absorption spectra and Tauc plot analyses were conducted after exposure to 1000 ppm of $NH_3$. As shown in Figure S3b, the absorbance in the 300–450 nm range decreases significantly following $NH_3$ exposure, indicating a substantial disruption in the light-absorption capability of the film. After recovery in ambient air, the absorption increased slightly but did not fully return to the pristine level, suggesting a degree of irreversible change in the optical characteristics of the film. The corresponding Tauc plots depicted in Figure S3c provide further insight into the bandgap evolution. The optical bandgap of the pristine film was 2.83 eV, which increased to 2.93 eV upon $NH_3$ exposure. After the recovery process, the bandgap decreased to 2.87 eV. This irreversible bandgap widening is consistent with the structural changes observed via SEM and XRD analyses, implying that high $NH_3$ concentrations can permanently alter the electronic structure of $FA_3Sb_2Br_9$ films.

Fourier transform infrared (FT-IR) spectroscopy was employed to investigate the changes in the organic functional groups of the $FA_3Sb_2Br_9$ thin films upon exposure to $NH_3$ gas. As shown in Figure 2d, most of the vibrational bands remained unchanged regardless of $NH_3$ treatment. However, distinct variations were observed in the regions associated with NH bonding. Specifically, the broad absorption bands in the range of 3500–3300 $cm^{-1}$, corresponding to N—H stretching vibrations, and 1650–1580 $cm^{-1}$, associated with N—H bending vibrations, became more pronounced after $NH_3$ exposure. This increase in intensity suggests that $NH_3$ molecules were chemisorbed onto the surface of $FA_3Sb_2Br_9$, forming hydrogen bonds or engaging in surface interactions with the available sites. After recovery in ambient air, the intensities of these N—H-related peaks decreased, implying that the chemisorbed $NH_3$ molecules were partially desorbed from the film surface. This reversible chemisorption behavior was consistent with the optical and morphological observations. A similar trend was observed for the films exposed to a higher $NH_3$ concentration (1000 ppm; Figure S3d), further validating the surface interaction mechanism between $FA_3Sb_2Br_9$ and $NH_3$.

X-ray photoelectron spectroscopy (XPS) spectra were obtained to examine the chemical bonding states and elemental compositions of the pristine, $NH_3$-exposed, and recovered $FA_3Sb_2Br_9$ thin films, as shown in Figures 2e,f and S4. The XPS spectrum (Figure S4a) confirmed the presence of C, N, Br, and Sb in all the film states. Figure 2e shows high-resolution Br 3*d* spectra, where the pristine sample exhibits a single Br 3*d* peak centered at 66.4 eV. Upon exposure to $NH_3$, this peak splits into two distinct components at 66.4 and 65.7 eV, indicating a chemical shift of −0.7 eV. This shift suggests a change in the local chemical environment of the Br atoms owing to $NH_3$ interactions. After recovery, the Br 3*d* peak partially shifted back to 65.98 eV, implying a partial reversal of the chemical state. Similarly, the high-resolution Sb 3*d* spectra (Figure S4b) show that the pristine peaks located at 537.7 eV (Sb $3d_{3/2}$) and 528.4 eV (Sb $3d_{5/2}$) shift to 537.3 and 527.9 eV after $NH_3$ exposure, followed by a recovery to 537.6 and 528.1 eV, respectively, after ambient recovery. These results indicate reversible electron density modulation around the Sb atoms upon $NH_3$ chemisorption and desorption. Figure S4c displays the C 1*s* spectra, where the peak at 284.2 eV, which is attributed to C in the FA cation, decreases in intensity after $NH_3$ exposure. This suggests possible surface interactions between $NH_3$ and the FA molecule. Upon recovery, the C 1*s* peak regained some of its original intensity, which is consistent with the desorption of $NH_3$. For the N 1s region, Figure S4d shows negligible binding energy shifts, with values around 398.0 eV across all samples, indicating that the chemical state of N in FA remains largely unaffected. However, Figure 2f shows an increase in the peak intensity of N 1*s* after $NH_3$ exposure, followed by a decrease after recovery. This trend supports the conclusion that the $NH_3$ molecules were chemisorbed onto the $FA_3Sb_2Br_9$ surface and partially desorbed upon exposure to air, which is consistent with the FT-IR results.

## 2.2 | Gas-Sensing Study of $FA_3Sb_2Br_9$ Thin Films

Figure 3a shows the fully saturated transient response of the $FA_3Sb_2Br_9$ thin film-based sensor upon exposure to 100 ppm $NH_3$ under a constant bias voltage of 1 V. Upon $NH_3$ gas introduction, the response increased rapidly and reached a stable saturation region before gradually recovering to the baseline level after switching back to air. The gas response ($R = \Delta I/(I_t - I_{air})/I_{air} \times 100$ (%)) reached approximately 235% at 100 ppm $NH_3$ concentration, with response and recovery times of 13 and 289 s, respectively, calculated at the 90% threshold level. The observed response amplification likely originates from enhanced p-type carrier modulation induced by $NH_3$ incorporation in $FA_3Sb_2Br_9$, which will be discussed in detail later. The clearly defined and repeatable switching behavior demonstrates the reversible interaction between $NH_3$ and the $FA_3Sb_2Br_9$ film, highlighting its strong potential for reliable chemiresistive $NH_3$-sensing applications.

To systematically assess the $NH_3$-sensing performance of the $FA_3Sb_2Br_9$-based sensor, dynamic response and recovery curves were recorded for $NH_3$ concentrations ranging from 1 to 10 ppm (Figure 3b). The sensor exhibited clear and distinguishable responses even at low concentrations, with a consistent signal increase and recovery trend for each $NH_3$ injection cycle.

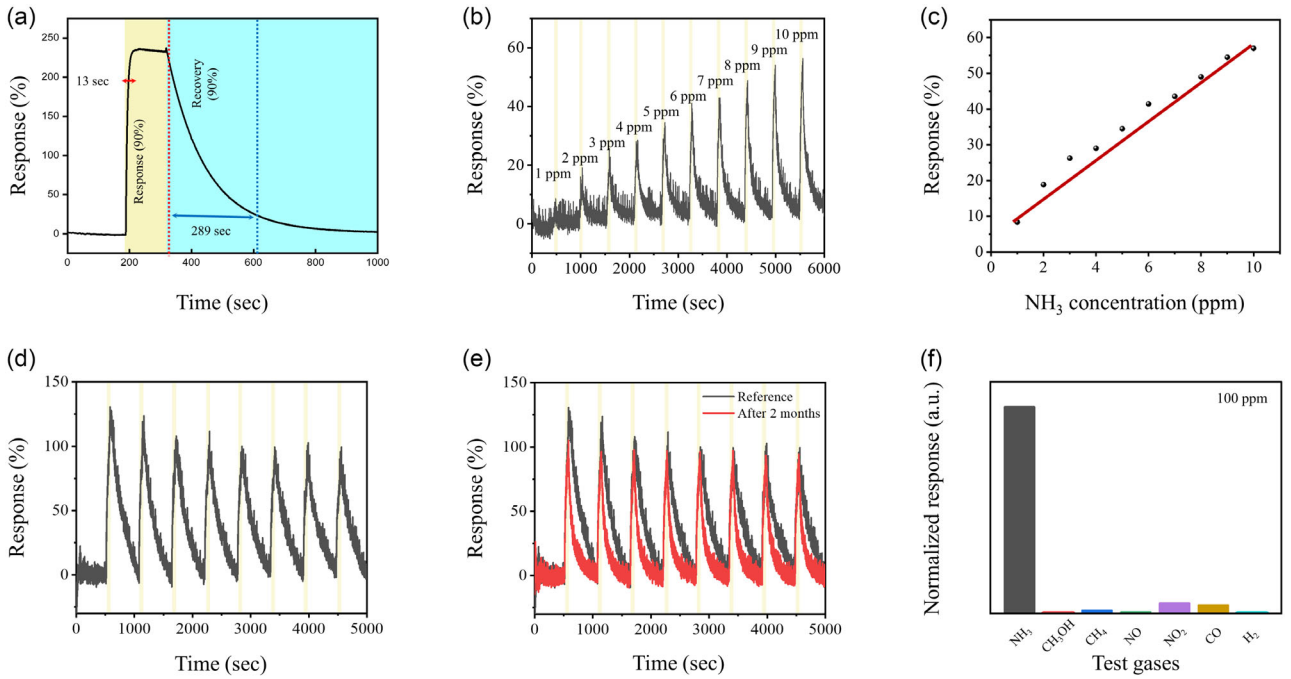


**FIGURE 3** | Gas-sensing performance of the $FA_3Sb_2Br_9$ thin film-based $NH_3$ sensor under ambient conditions: (a) response–recovery curve to 100 ppm $NH_3$ at 1 V bias. (b) Response–recovery curves at various $NH_3$ concentrations (1–10 ppm). (c) Linear calibration curve showing sensor response versus $NH_3$ concentration. (d) Repeatability at 100 ppm $NH_3$. (e) Long-term stability comparison between initial and 2-month-stored sensors (100 ppm $NH_3$, 20%–25% RH). (f) Selectivity against different gases (all at 100 ppm) including $NH_3$, MeOH, $CH_4$, NO, $NO_2$, CO, and $H_2$.

Remarkably, the sensor demonstrated a detectable response at 1 ppm, suggesting a low limit of detection (LOD), with the potential for sub-ppm level (0.1–1.0 ppm) $NH_3$ detection. To quantify this relationship, Figure 3c presents a calibration curve plotting the sensor response as a function of the $NH_3$ concentration. A strong linear correlation was observed ($R^2 \approx 0.99$), indicating that the response increases proportionally with $NH_3$ concentration in the tested range. This linearity, combined with high sensitivity, excellent repeatability, and low LOD, highlights the potential of $FA_3Sb_2Br_9$ as a promising candidate for quantitative $NH_3$ sensing in practical environments. To further verify the dynamic electrical sensing behavior, the corresponding raw current–time transient curves measured under 40, 60, and 100 ppm $NH_3$ are provided in Figure S5, Supporting Information. The raw data clearly show stable baseline current characteristics, distinct current increases upon $NH_3$ exposure, and gradual recovery after air purging.

Repeatability is a crucial performance parameter for evaluating the reliability of gas sensors for real-world applications. To assess this, the $FA_3Sb_2Br_9$-based sensor was subjected to eight consecutive exposure–recovery cycles under 100 ppm $NH_3$ at room temperature, and the corresponding dynamic response curves are shown in Figure 3d. The sensor consistently exhibited sharp response and recovery transitions with minimal variations in the peak values and kinetics across cycles, confirming its excellent repeatability and operational reproducibility. Figure S6 shows the results of the repeatability test conducted at a low $NH_3$ concentration (10 ppm). The sensor maintained a consistent response amplitude of approximately 40% across five consecutive cycles, further demonstrating its reliable performance even at reduced analyte concentrations. These results collectively confirm the high reproducibility of the $FA_3Sb_2Br_9$ thin film-based sensor under various $NH_3$ concentrations.

To further assess device reliability, long-term stability was investigated by storing the fabricated sensors in a desiccator under ambient laboratory conditions (relative humidity: 20%–25%) for 2 months. As shown in Figure 3e, the sensing response to 100 ppm $NH_3$ after storage retains approximately 97% of its original response level when averaged over eight repeated cycles, compared to the initial measurement. The overlapping response profiles before and after storage demonstrated the high durability and chemical stability of the sensor under ambient storage conditions, which are essential for practical deployment in environmental monitoring applications. Furthermore, to evaluate the influence of moisture on the $NH_3$-sensing behavior under practical environmental conditions, additional sensing measurements were conducted at different relative humidity levels ranging from 0% to 60% RH at a fixed $NH_3$ concentration of 40 ppm and 85°C. As shown in Figure S7, the sensor response gradually increased with increasing humidity level, indicating that moisture affects the $NH_3$-sensing characteristics of the $FA_3Sb_2Br_9$ sensor, likely through enhanced ionic interaction and charge transport modulation under humid conditions.

A crucial requirement for practical $NH_3$ sensors is high selectivity toward $NH_3$ over other interfering gases. To demonstrate the selectivity of the $FA_3Sb_2Br_9$-based sensor, its response to 100 ppm of various test gases was compared. These gases include $NH_3$, MeOH, $CH_4$, NO, $NO_2$, CO, and $H_2$, as shown in Figure 3f. The normalized response values for each gas were 1.00 for $NH_3$, 0.11 for MeOH, 0.33 for $CH_4$, 0.29 for NO, 0.65 for $NO_2$, 0.52 for CO, and 0.09 for $H_2$. MeOH, $CH_4$, NO, and $H_2$ exhibited negligible responses compared to $NH_3$. Although $NO_2$ and CO produced relatively high responses, the signal for $NH_3$ was still approximately 20 times greater than that of the next-highest gas, indicating a strong preferential response. These results demonstrate that the $FA_3Sb_2Br_9$ thin film-based gas sensor possesses excellent selectivity toward $NH_3$, making it a promising candidate for targeted $NH_3$ detection in complex gas environments. This excellent selectivity, along with the overall sensing performance, was further underscored by comparison with other halide perovskite-based gas sensors, as summarized in Table S1.

## 2.3 | Proposed Sensing Mechanism

Density functional theory (DFT) calculations were performed to elucidate the sensing mechanism of $FA_3Sb_2Br_9$ toward $NH_3$. Two possible mechanisms were considered: (1) $NH_3$ molecule incorporation into the perovskite bulk and (2) surface adsorption [30, 37]. In the bulk incorporation model, $NH_3$ was assumed to substitute for an FA cation site, which has been identified as a likely incorporation site in the literature [38]. In addition, the splitting of the Br 3*d* XPS peak upon $NH_3$ exposure suggests the incorporation of $NH_3$ at FA sites. The optimized atomic configurations of $FA_3Sb_2Br_9$ with and without $NH_3$ substitution are shown in Figure 4a. The electronic band structure and projected density of states (PDOS) of the pristine $FA_3Sb_2Br_9$ are shown in Figure 4b. The valence band is primarily composed of Br 4*p* orbitals, whereas the conduction band arises from the hybridization of the Sb 5*p* and Br 4*p* states. After $NH_3$ incorporation, as shown in Figure 4c, the Fermi level shifts below the valence band maximum (VBM), indicating the introduction of hole states and the formation of p-type doping behavior. The defect level formed below the VBM acted as an acceptor state capable of capturing valence electrons, thereby facilitating hole generation. This indicates that $NH_3$ substitution at the FA site effectively acted as a p-type dopant. These findings are consistent with previous reports that Sb-based bromide perovskites inherently exhibit p-type conductivity owing to native defects [39].

To verify the enhancement of p-type doping upon $NH_3$ incorporation, contact potential difference (CPD) measurements were conducted using Kelvin probe force microscopy (KPFM) under dark conditions. CPD is defined as the difference in work function between the atomic force microscopy (AFM) tip and the sample surface and serves as an indirect indicator of the surface electronic properties [34, 40]. Figure 5 shows the topography and CPD measurements of pristine, $NH_3$-exposed (100 ppm), and recovered films. As shown in the AFM images (Figure 5a–c), $NH_3$ exposure transforms the voids into a flower-like pattern, which is consistent with the SEM results. The film roughness increased from that of the pristine sample to that of the recovered samples (Figure 5g). The CPD maps (Figure 5d–f) reveal a substantial drop in the average CPD values after $NH_3$ exposure (Figure 5h), indicating a downward shift in the Fermi level relative to the AFM tip. This shift is consistent with the increased p-type character at the surface owing to $NH_3$-induced doping. These experimental findings corroborate the DFT simulation results discussed earlier and are supported by previous

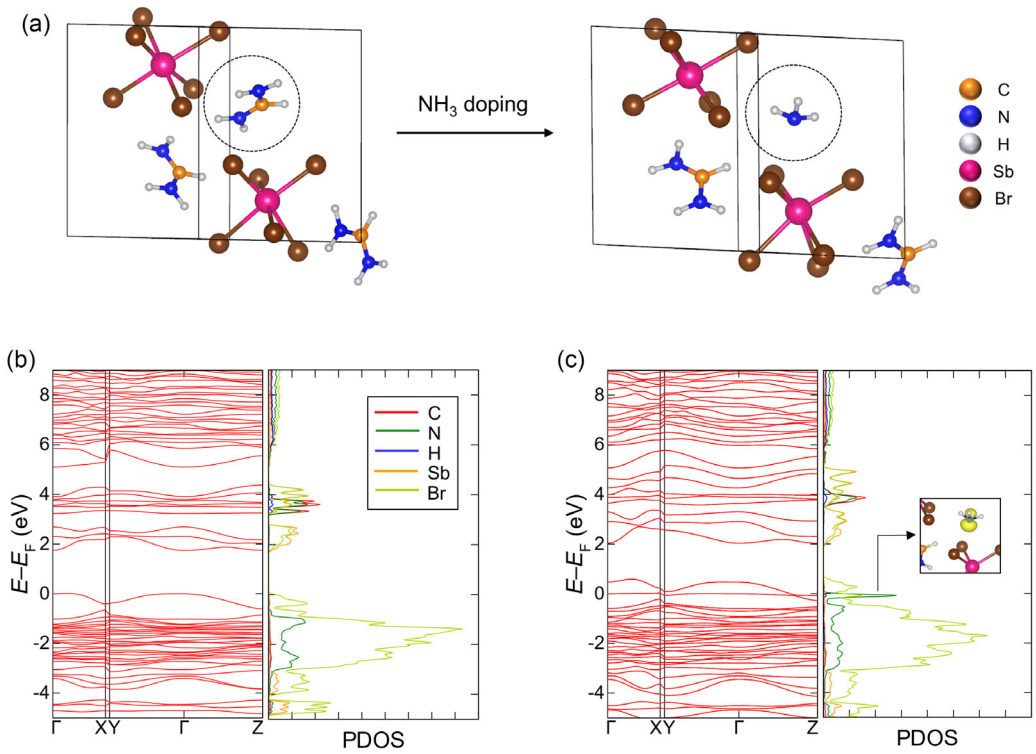


**FIGURE 4** | DFT calculations illustrating the proposed $NH_3$-sensing mechanism of $FA_3Sb_2Br_9$: (a) optimized atomic structures of pristine (left) and $NH_3$-incorporated (right) $FA_3Sb_2Br_9$, where $NH_3$ substitutes a FA site. Electronic band structure and PDOS of (b) pristine $FA_3Sb_2Br_9$ and (c) $NH_3$-substituted $FA_3Sb_2Br_9$. $E_F$ indicates the Fermi level. The inset of (c) represents the charge-density distribution of the defect state.

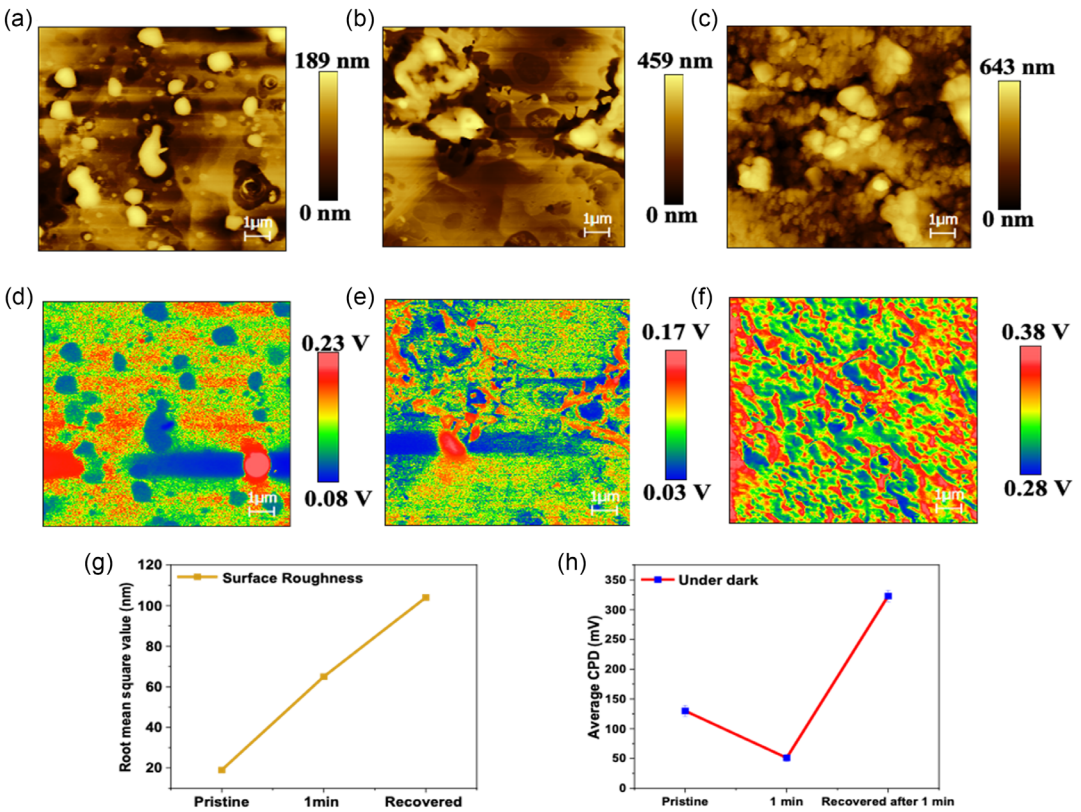


**FIGURE 5** | Morphology and KPFM characterization of $FA_3Sb_2Br_9$ thin films under dark conditions. (a)–(c) AFM topographic images of pristine, $NH_3$-exposed (100 ppm), and recovered films. (d)–(f) Corresponding CPD maps obtained by KPFM. (g) Surface roughness and (h) average CPD values for each film (error bars represent standard deviations).

reports [41, 42]. We notice that the recovered film exhibited a higher CPD value than the pristine film, which may be attributed to irreversible (or kinetically sluggish) changes in the surface morphology and microstructure left in the film, aligning with the absorption and other spectroscopy data. Interestingly, the recovered film exhibited a higher CPD value than the pristine film, which may be attributed to irreversible changes in the surface morphology and microstructure. This observation aligns with the differences observed in the UV–visible absorption and SEM results, suggesting that although partial recovery occurs, the postexposure film does not fully revert to its original state [42].

Although the dark KPFM results, together with the DFT calculations, indicate that $NH_3$ incorporation induces p-type doping, photogenerated carriers could, in principle, also alter the surface potential and influence CPD values. To exclude this possibility and confirm that the observed CPD shift originates solely from chemical interactions, light-dependent CPD measurements were performed using KPFM as a control experiment. As shown in Figure S8, a series of AFM and KPFM measurements were conducted under three different illumination conditions: dark, red LED (620 nm), and blue LED (490 nm). Under red and blue light irradiation, no significant changes in the CPD values were observed for any of the samples (pristine, $NH_3$-exposed, or recovered) compared with the measurements obtained under dark conditions. This absence of CPD modulation under photoillumination suggests that photogenerated carriers do not significantly contribute to the surface potential modulation in these films. Therefore, the light-induced doping mechanism can be ruled out. These results strongly support the conclusion that $NH_3$ incorporation is responsible for the observed p-type doping behavior, reinforcing the view that $NH_3$ acts as a chemical dopant rather than an optical trigger, thereby enhancing the hole density through chemical interactions with the film matrix. To facilitate quantitative comparison, the average CPD values under dark, red LED, and blue LED illumination conditions were extracted (Figure S9). Across all measurement conditions, no significant variation in the CPD was observed for any of the films.

The electrical behavior associated with the $NH_3$-induced doping was further investigated by conductive AFM (CAFM) performed under dark conditions with an applied bias of +3 V. As shown in Figure S10, the current sharply increases from pA to nA on the $NH_3$-exposed film and then decreases to its initial level upon recovery. These results provide direct nanoscale evidence of the enhanced hole conductivity induced by $NH_3$ exposure, supporting the proposed p-type doping mechanism. The reversible change in the local current response further demonstrates that the conductivity modulation is chemically triggered rather than permanent, which is in line with the bulk doping behavior inferred from DFT calculations and CPD measurements.

Conversely, to examine the second sensing mechanism involving $NH_3$ surface adsorption, the DFT calculations were conducted for three representative surface terminations of $FA_3Sb_2Br_9$: SbBr, FA, and vacancy termination. In each case, $NH_3$ molecules were adsorbed onto the surface and the resulting electronic band structures were compared with those of the pristine surfaces (Figure S11). No significant changes were observed near the conduction band minimum or valence band maximum after $NH_3$ adsorption. The bandgap remained nearly unchanged across all surface configurations upon $NH_3$ adsorption. These results indicate that $NH_3$ surface adsorption does not notably affect the electronic structure or carrier concentration and is therefore unlikely to contribute substantially to the sensing behavior. This finding supports the conclusion that the primary sensing mechanism in $FA_3Sb_2Br_9$ arises from the bulk incorporation of $NH_3$, rather than surface adsorption.

## 3 | Conclusion

This study highlights the potential of $FA_3Sb_2Br_9$ thin film-based sensors, a novel and Pb-free material that has not been previously reported for the detection of $NH_3$ gas. The sensors exhibited a significant increase in current upon $NH_3$ exposure, with a calculated gas response ($R$) of 235% at 100 ppm, and demonstrated rapid response and recovery times of 13 and 289 s, respectively. Excellent repeatability was confirmed through consistent response and recovery over multiple cycles. Furthermore, the sensors demonstrated a low LOD, indicating their capability to detect $NH_3$ at a concentration of approximately 1 ppm. The linear relationship between the $NH_3$ concentration and sensor response underscores its suitability for quantitative gas-sensing applications. Selectivity tests revealed that the $FA_3Sb_2Br_9$ sensors had a significantly higher response to $NH_3$ than to other gases such as MeOH, $CH_4$, NO, $NO_2$, CO, and $H_2$, highlighting their specific responsiveness to $NH_3$. Long-term stability tests indicated that the sensors retained approximately 97% of their initial performance after 2 months of storage under ambient conditions, demonstrating excellent durability and reliability. Overall, the $FA_3Sb_2Br_9$ thin film-based sensors utilizing a novel material exhibit high sensitivity, excellent selectivity, and robust long-term stability for $NH_3$ detection, making them promising candidates for practical gas-sensing applications. In addition, valuable insights into the sensing mechanism were provided by DFT calculations, which were employed to support the experimental findings and confirm the role of $NH_3$-induced p-type doping as the dominant sensing pathway.

## 4 | Experimental Section

### 4.1 | Materials

Formamidinium bromide (FABr) was purchased from Greatcell Solar (Queanbeyan, Australia). Antimony(III) bromide ($SbBr_3$, 99%) was purchased from Alfa-Aesar (Haverhill, MA, USA). *N*,*N*-Dimethylformamide (DMF, 99.8%) was purchased from Sigma–Aldrich (Burlington, MA, USA).

### 4.2 | Preparation of $FA_3Sb_2Br_9$ Precursor Solution

An FABr-$SbBr_3$ (FABr:$SbBr_3$ molar ratio of 3:2) solution was prepared using DMF. The precursor concentration was 0.5 M. The precursor solution was stirred at 70°C for approximately 1 h until it was completely dissolved in a clear yellow solution. The dissolved solution was filtered using a 0.45 μm pore size PTFE filter before deposition of perovskites films.

### 4.3 | Fabrication of $FA_3Sb_2Br_9$-Based $NH_3$ Gas Sensor

The glass substrates were sequentially washed with acetone and isopropanol in an ultrasonic bath for 10 min in each solvent. The washed substrates were dried in an oven for 5 min and subjected to UV–ozone treatment for 10 min. The preparation process of the $FA_3Sb_2Br_9$ thin film is illustrated in Figure 1a. The prepared $FA_3Sb_2Br_9$ solution was spin-coated onto washed glass substrates at 2000 rpm for 60 s. The $FA_3Sb_2Br_9$ film was annealed at 150°C for 10 min, and the resulting thin film was observed at the right end of the hot plate (Figure 1a). The devices were fabricated via thermal evaporation, utilizing a finger mask, and depositing a layer of Au (approximately 80 nm) on the thin films as the electrode.

### 4.4 | Characterization

All structural and spectroscopic characterizations presented in Figure 2, including SEM, XRD, UV–visible absorption, FT-IR, and XPS analyses, were performed ex situ after controlled $NH_3$ exposure and recovery treatments. For the preparation of $NH_3$-exposed samples, the $FA_3Sb_2Br_9$ thin films were exposed to 100 ppm $NH_3$ gas at a flow rate of 500 sccm at 70°C for 60 s in a sealed chamber prior to ex situ characterization. The recovered samples were obtained by subsequently exposing the $NH_3$-treated films to high-purity air at the same flow rate and temperature for 500 s prior to characterization measurements. For characterization, $NH_3$-exposed $FA_3Sb_2Br_9$ thin films were subjected to a flow rate of 500 sccm, $cm^{-3}$ $min^{-1}$ of 100 ppm $NH_3$ gas in a chamber at 70°C for 60 s. The recovered $FA_3Sb_2Br_9$ thin films, previously exposed to $NH_3$ at a flow rate of 500 sccm of high-purity air, were aerated in the chamber at 70°C for 500 s. The images of the $NH_3$-exposed and recovered films are shown in Figure 1b. The surface morphologies and elemental distributions of the $FA_3Sb_2Br_9$ films were analyzed using SEM (JSM-6610LV, JEOL, Tokyo, Japan) combined with EDS. XRD patterns were obtained using an X-ray diffractometer (Empyrean, PANalytical, Malvern, UK; Cu Kα radiation source at $\lambda = 1.54$ Å) under a voltage of 40 kV and current of 40 mA in a 2° angle range of 10°–60°. The UV–visible absorption spectra were recorded using a UV–vis–NIR spectrophotometer (Cary 5000, AGILENT Technologies, Santa Clara, CA, USA). The infrared spectra of the samples were recorded using FT-IR (Nicolet iS10, Thermo Scientific, Waltham, MA, USA) spectroscopy. XPS was conducted with a modified XPS system (ESCALab MK II, VG Scientific, Conroe, TX, USA) and an Al Kα X-ray source (1486.6 eV) at a high voltage of 14 kV and a beam current of 30 mA.

The gas-sensing performance of the $FA_3Sb_2Br_9$ thin film-based sensor was evaluated using a gas-sensing setup equipped with a chamber (VPX-G400, WIT) with both inlet and outlet valves. $NH_3$ gas and high-purity air were injected into the chamber using a mass-flow controller (GMC1200, ATOVAC, Gyeonggi-do, Korea). The sample was mounted on a stage holder within the chamber and connected to a source meter (Keithley 2450 SMU) interfaced with a computer. The sensing properties of the perovskite samples were evaluated by exposing them to $NH_3$ gas mixed with air. Current measurements were performed using a source meter interfaced with a computer, with the sensor operating at 70°C under a bias voltage of 1 V. The concentrations of gases used to evaluate the selectivity of the gas sensor, such as methanol (MeOH), methane ($CH_4$), $NO_x$, CO, and hydrogen ($H_2$), were 100 ppm and were extracted from the gas cylinders. The current variation in the $FA_3Sb_2Br_9$ thin film-based sensor was measured after exposure to different concentrations of $NH_3$ between 1 and 100 ppm. To demonstrate the repeatability of the gas sensor, current values from multiple cycles were measured under the same $NH_3$ concentration and measurement conditions. Long-term stability was investigated by examining the responsiveness of the device several months after manufacturing.

Gas response ($R$) was defined as $R = \Delta I(I_t - I_{air})/I_{air} \times 100$ (%), where $I_t$ and $I_{air}$ indicate the current in real-time and in air, respectively. The response and recovery times were defined as the times required for the sensor to achieve 90% of the total current change during adsorption and desorption, respectively.

The AFM system, specifically the AIST-NT SmartSPM1000 model, was utilized to perform KPFM and CAFM measurements. All the KPFM measurements were performed using a platinum-coated AFM tip (HQ:NSC35/Pt). The resonance frequency of the tip was 150 kHz, with a force constant of 5.4 N/m. A controlled N-filled chamber was used to reduce the effects of the external environmental factors. Each sample was cleaned under a N stream before the experiment to remove external contamination. A small 0.7 Hz scanning rate was used to achieve a high resolution of the images and to minimize artifacts from the samples. For the light measurements, two external LEDs (blue and red) were used with the same illumination value. The LEDs were mounted at an angle of 30° to avoid any shadows from probes on the samples. Different areas of each sample were scanned to verify the reproducibility and authenticity of the analyses. A platinum-coated AFM tip (HQ:NSC38/PT) with a force constant of 5.4 N/m was used for the CAFM measurements in the contact mode. A small nanoforce of a few nano newtons (nN) was used to ensure that the tip and sample surface were in consistent contact. All measurements were performed in the dark by applying a +3V bias voltage to ensure data consistency. All measurements were carefully monitored to ensure consistent experimental conditions and enhance reliability by examining multiple regions of the same sample.

### 4.5 | Computational Method

Spin-polarized DFT calculations were performed using the Vienna Ab-initio Simulation Package with the projector-augmented wave pseudopotential to represent core–valence interactions [43]. Geometry optimization was conducted by employing the generalized gradient approximation with the Perdew–Burke–Ernzerhof functional [44]. Van der Waals effects were considered using Grimme's D3-dispersion correction [39]. A plane-wave basis set with a cutoff energy of 300 eV was used. The convergence criteria for energy and force were set to $10^{-5}$ eV and 0.02 eV/Å, respectively. For Brillouin zone integration, we sampled a Γ-centered $4 \times 4 \times 4$ k-point grid.

#### Author Contributions

J.H.K. performed the analyses and wrote the overall paper; G.L. performed the experiments and analyses of the part of $NH_3$ gas detection;

H.J. performed the analyses of the part of the computational simulation; Y.K. and C.K. performed the experiments of the part of the perovskite thin films; J.K. (Jongbok Kim) and J.K. (Jinsung Kwak) guided and interpreted the part of the perovskite thin films; T.Y., J.S., and J.K. (Jincheol Kim) guided and interpreted the part of $NH_3$ gas detection; H.W.L. reviewed and edited this paper; Y.K. reviewed and edited the computational characteristics of $NH_3$-sensing mechanism of perovskite; M.S. designed, directed, and supervised this paper. J.H.K., G.L., and H.J. contributed equally to this project. All the authors have read the paper and have agreed to its publication. I would like to declare on behalf of my co-authors that the work described was original research that has not been published previously, and not under consideration for publication elsewhere, in whole or in part.


## Acknowledgments

This research was supported by the Fundamental Research Program (PNKA460) of the Korea Institute of Materials Science (KIMS), the Korea Institute of Energy Technology Evaluation and Planning (KETEP), the Ministry of Trade, Industry & Energy (MOTIE) of the Republic of Korea (No. RS-2024-00437030), and the National Research Foundation of Korea (NRF) grant funded by the Korea government (MSIT) (RS-2024-00406152, RS-2024-00444460).


## Conflicts of Interest

The authors declare no conflicts of interest.

## Data Availability Statement

The data that support the findings of this study are available from the corresponding author upon reasonable request.

## References


1. W. Nie, H. Tsai, R. Asadpour, et al., "High-Efficiency Solution-Processed Perovskite Solar Cells with Millimeter-Scale Grains," *Science* 347 (2015): 6221.

2. M. I. Saidaminov, V. Adinolfi, R. Comin, et al., "Planar-Integrated Single-Crystalline Perovskite Photodetectors," *Nature Communications* 6 (2015): 8724.

3. D. Liu, Y. Wang, H. Xu, et al., "$SnO_2$-Based Perovskite Solar Cells: Configuration Design and Performance Improvement," *Solar RRL* 3 (2019): 1800292.

4. A. D. Sheikh, A. P. Patil, S. S. Mali, C. K. Hong, and P. S. Patil, "New Insights into Active-Area-Dependent Performance of Hybrid Perovskite Solar Cells," *Journal of Materials Science* 54 (2019): 10825–10835.

5. N. Gupta, O. Nanda, R. Grover, and K. Saxena, "A New Inorganic–organic Hybrid Halide Perovskite Thin-Film Based Ammonia Sensor," *Organic Electronics* 58 (2018): 202–206.

6. A. K. Nayak, R. Ghosh, S. Santra, P. K. Guha, and D. Pradhan, "Hierarchical Nanostructured $WO_3$-$SnO_2$ for Selective Sensing of Volatile Organic Compounds," *Nanoscale* 7 (2015): 12460–12473.

7. G. Maculan, A. D. Sheikh, A. L. Abdelhady, et al., "$CH_3NH_3PbCl_3$ Single Crystals: Inverse Temperature Crystallization and Visible-Blind UV Photodetector," *Journal of Physical Chemistry Letters* 6 (2015): 3781–3786.

8. K. Ren, L. Huang, S. Yue, et al., "Turning a Disadvantage into an Advantage: Synthesizing High-Quality Organometallic Halide Perovskite Nanosheet Arrays for Humidity Sensors," *Journal of Materials Chemistry C* 5 (2017): 2504–2508.

9. D. Lee, S.-J. Lee, J. H. Kim, et al., "Multimodal Gas Sensor Detecting Hydroxyl Groups with Phase Transition Based on Eco-Friendly Lead-Free Metal Halides," *Advanced Functional Materials* 32 (2022): 2202207.

10. N. Ding, D. Zhou, G. Pan, et al., "Europium-Doped Lead-Free $Cs_3Bi_2Br_9$ Perovskite Quantum Dots and Ultrasensitive $Cu^{2+}$ Detection," *ACS Sustainable Chemistry and Engineering* 7 (2019): 8397–8404.

11. A. I. Ayesh, S. A. Alghamdi, B. Salah, S. H. Bennett, C. Crean, and P. J. Sellin, "High Sensitivity $H_2S$ Gas Sensors Using Lead Halide Perovskite Nanoparticles," *Results in Physics* 35 (2022): 105333.

12. M. A. Stoeckel, M. Gobbi, S. Bonacchi, et al., "Reversible, Fast, and Wide-Range Oxygen Sensor Based on Nanostructured Organometal Halide Perovskite," *Advanced Materials* 29 (2017): 1702469.

13. W. Ye, J.-H. He, Q. Cao, et al., "Surfactant-Free, One-Step Synthesis of Lead-Free Perovskite Hollow Nanospheres for Trace CO Detection," *Advanced Materials* 33 (2021): 2100674.

14. V. X. Hien, P. D. Hoat, P. T. Hung, S. Lee, J. H. Lee, and Y. W. Heo, "Room-Temperature $NO_2$ Sensor Based on a Hybrid Nanomaterial of Methylammonium Tin Iodide Submicron Spheres and Tin Dioxide Nanowires," *Scripta Materialia* 188 (2020): 107–111.

15. Y. Zhao and K. Zhu, "Optical Bleaching of Perovskite $(CH_3NH_3)PbI_3$ through Room Temperature Phase Transformation Induced by Ammonia," *Chemical Communications* 50 (2014): 1605–1607.

16. W. Jiao, J. He, and L. Zhang, "Synthesis and High Ammonia Gas Sensitivity of $(CH_3NH_3)$ $PbBr_{3-x}I_x$ Perovskite Thin Film at Room Temperature," *Sensors and Actuators B: Chemical* 309 (2020): 3111–3117.

17. H. Lesmana, Z. Zhang, X. Li, M. Zhu, W. Xu, and D. Zhang, "$NH_3$ as a Transport Fuel in Internal Combustion Engines: A Technical Review," *Journal of Energy Resources Technology* 141 (2019): 7.

18. T. W. Sung and Y. L. Yo, "Ammonia Vapor Sensor Based on CdSe/$SiO_2$ Core-Shell Nanoparticles Embedded in Sol-Gel Matrix," *Sensors and Actuators B: Chemical* 188 (2013): 702–708.

19. G. S. Li, W. Q. Zhan, C. K. She, et al., "Stable Fluorescent $NH_3$ Sensor Based on $MAPbBr_3$ Encapsulated by Tetrabutylammonium Cations," *Journal of Alloys and Compounds* 835 (2020): 155386–155393.

20. S. Bathrinath, J. Devaganesh, B. Santhi, and S. Saravanasankar, "The Adverse Human Health Effects due to Ammonia, Hydrogen Sulphide and Chlorine in Process Industry: A Review," *IJMPERD* 8 (2018): 394–402.

21. X. Tang, M. Debliquy, D. Lahem, Y. Yan, and J.-P. Raskin, "A Review on Functionalized Graphene Sensors for Detection of Ammonia," *Sensors* 21 (2021): 1443.

22. Y. Xu, Y. Wang, Z. Lei, C. Wang, X. Meng, and P. Cheng, "MXene-Based Gas Sensors for $NH_3$ Detection: Recent Developments and Applications," *Micromachines* 16 (2025): 820.

23. M. Chaparia, R. K. C. Deepak, and U. K. Dwivedi, "Metal Oxide Semiconductors for Gas Sensors: A Comprehensive Review of Materials, Mechanisms, and Performance," *Materials Science in Semiconductor Processing* 204 (2026): 110280.

24. S. K. Sharma, C. Phadnis, T. K. Das, et al., "Reversible Dimensionality Tuning of Hybrid Perovskites with Humidity: Visualization and Application to Stable Solar Cells," *Chemistry of Materials* 31 (2019): 3111–3117.

25. E. Mosconi, J. M. Azpiroz, and F. De Angelis, "Ab Initio Molecular Dynamics Simulations of Methylammonium Lead Iodide Perovskite Degradation by Water," *Chemistry of Materials* 27 (2015): 4885–4892.

26. N. H. Nickel, F. Lang, V. V. Brus, O. Shargaieva, and J. Rappich, "Unraveling the Light Induced Degradation Mechanisms of $CH_3NH_3PbI_3$ Perovskite Films," *Advanced Electronic Materials* 3 (2017): 1700158.

27. D. H. Fabini, R. Seshadri, and M. G. Kanatzidis, "The Underappreciated Lone Pair in Halide Perovskites Underpins Their Unusual Properties," *MRS Bulletin* 45 (2020): 467–477.

28. Z. Jin, Z. Zhang, J. Xiu, H. Song, T. Gatti, and Z. He, "A Critical Review on Bismuth and Antimony Halide Based Perovskites and Their Derivatives for Photovoltaic Applications: Recent Advances and Challenges," *Journal of Materials Chemistry A* 8 (2020): 16166–16188.

29. Y.-Q. Hu, H.-Y. Hui, W.-Q. Lin, H.-Q. Wen, D.-S. Yang, and G.-D. Feng, "Crystal and Band-Gap Engineering of One-Dimensional Antimony/Bismuth-Based Organic–Inorganic Hybrids," *Inorganic Chemistry* 58 (2019): 16346–16353.

30. W. Jiao, J. He, and L. Zhang, "Fabrication and Investigation of a New All-Inorganic Lead Free Perovskite $Cs_3Bi_2I_6Br_3$ for Ammonia Detection at Room Temperature," *Journal of Alloys and Compounds* 895 (2022): 162561.

31. G. Kresse and J. Furthmuller, "Effcient Iterative Schemes for Ab Initio Total-Energy Calculations Using a Plane-Wave Basis Set," *Physical Review B* 54 (1996): 11169.

32. J. P. Perdew, K. Burke, and M. Ernzerhof, "Generalized Gradient Approximation Made Simple," *Physical Review Letters* 77 (1997): 1396.

33. S. Grimme, S. Ehrlich, and L. Goerigk, "Effect of the Damping Function in Dispersion Corrected Density Functional Theory," *Journal of Computational Chemistry* 32 (2011): 1456–1465.

34. S. K. Shil, F. Wang, K. O. Egbo, et al., "Two-Step Chemical Vapor Deposition-Synthesized Lead-Free All-Inorganic $Cs_3Sb_2Br_9$ Perovskite Microplates for Optoelectronic Applications," *ACS Applied Materials and Interfaces* 13 (2021): 35930–35940.

35. M. G. Brik and I. V. Kityk, "Modeling of Lattice Constant and Their Relations with Ionic Radii and Electronegativity of Constituting Ions of $A_2XY_6$ Cubic Crystals (A=K, Cs, Rb, Tl; X=tetravalent Cation, Y=F, Cl, Br, I)," *Journal of Physics and Chemistry of Solids* 72 (2011): 1256–1260.

36. L. Dimesso, A. Quintilla, Y.-M. Kima, U. Lemmer, and W. Jaegermanna, "Investigation of Formamidinium and Guanidinium Lead Tri-Iodide Powders as Precursors for Solar Cells," *Materials Science and Engineering: B* 204 (2016): 27–33.

37. C. Bao, J. Yang, W. Zhu, et al., "A Resistance Change Effect in Perovskite $CH_3NH_3PbI_3$ Films Induced by Ammonia," *Chemical Communications* 51 (2015): 15426–15429.

38. J. Kim, L. Hu, H. Chen, et al., "P-Type Charge Transport and Selective Gas Sensing of All-Inorganic Perovskite Nanocrystals," *ACS Materials Letters* 2 (2020): 1368–1374.

39. M. K. Bhosale, A. I. Kazi, K. K. Pawar, et al., "Eco-Friendly $MA_3Bi_2I_9$ Perovskite Thin Films Based Ammonia Sensor," *Nanotechnology* 34 (2022): 065501.

40. M. Lee, L. Wang, D. Zhang, et al., "Scanning Probe Microscopy of Halide Perovskite Solar Cells," *Advanced Materials* 36 (2024): 2407291.

41. H. Shim, A. S. Sharma, R. Mishra, et al., "Probing Nanoscale Charge Transport Mechanisms in Quasi-2D Halide Perovskites for Photovoltaic Applications," *ACS Nano* 18 (2024): 31002–31013.

42. E. Choi, Y. Zhang, A. M. Soufiani, et al., "Exploration of Sub-Bandgap States in 2D Halide Perovskite Single-Crystal Photodetector," *npj 2D Materials and Applications* 6 (2022): 43.

43. R. Nie, R. R. Sumukam, S. Reddy, M. Banavoth, and S. I. Seok, "Lead-Free Perovskite Solar Cells Enabled by Hetero-Valent Substitutes," *Energy and Environmental Science* 13 (2020): 2363–2385.

44. Z. Kang, D. Zhang, T. Li, X. Liu, and X. Song, "Polydopamine-Modified $SnO_2$ Nanofiber Composite Coated QCM Gas Sensor for High-Performance Formaldehyde Sensing," *Sensors and Actuators: B. Chemical* 345 (2021): 130299.

## Supporting Information

Additional supporting information can be found online in the Supporting Information section.